Derived Over-Ocean Water Vapor Transports from Satellite-Retrieved $E - P$ Datasets

BYUNG-JU SOHN

School of Earth and Environmental Sciences, Seoul National University, Seoul, South Korea

ERIC A. SMITH

NASA Goddard Space Flight Center, Greenbelt, Maryland

FRANKLIN R. ROBERTSON

Global Hydrology and Climate Center, NASA Marshall Space Flight Center, Huntsville, Alabama

SEONG-CHAN PARK

School of Earth and Environmental Sciences, Seoul National University, Seoul, South Korea

(Manuscript received 14 July 2003, in final form 14 October 2003)

ABSTRACT

A methodology is developed for deriving atmospheric water vapor transports over the World Oceans from satellite-retrieved precipitation (P) and evaporation (E) datasets. The motivation for developing the method is to understand climatically varying properties of transports, that is, year-to-year changes of the seasonally averaged divergent transport distribution fields, over regions where conventional data, in particular, winds, are sparse. Ultimately, the method is intended to take advantage of the relatively complete and consistent coverage, as well as continuity in sampling, associated with $E - P$ datasets obtained from satellite measurements. Separate P and E retrievals from Special Sensor Microwave Imager (SSM/I) measurements, along with P retrievals from Tropical Rainfall Measuring Mission (TRMM) measurements, are used to obtain the transport solutions.

In this opening study, a 7-yr climatological normal is derived for the January–February–March (JFM) period for years 1988–94, providing the basis for comparing vapor transport anomalies from the 1997/98 El Niño and 1999/2000 La Niña events. These are derived from JFM-averaged transport solutions for 1998 and 1999, respectively. These two periods correspond to times when the Multivariate ENSO Index (MEI) provided by the NOAA Climatic Data Center (CDC) was first at a relative maximum and then at a relative minimum in conjunction with back-to-back west Pacific warm and cold events. Because the El Niño–La Niña events produce such highly contrasting behavior in the transports, shifting from a largely meridionally oriented solution to a largely zonally oriented solution, focusing on this pairing, helps to explain why the methodology is reliable and effective in capturing important details embedded in full-coverage $E - P$ fields.

The analysis includes a sensitivity study of the transport solution technique based on 20 combinations of four precipitation datasets (two satellite based and two model based) and five evaporation datasets (two satellite based, one in situ observation based, and two model based), which helps to explain the reliability of the method. The analysis also includes a comparison to water vapor transports derived with the same method, but applied to $E - P$ datasets obtained from global analysis products prepared by the National Centers of Environmental Prediction (NCEP), again to help explain the reliability of the method. The study concludes by first showing how the anomaly JFM 1998 El Niño solution behaves in close correspondence to associated SST anomalies and is generally more realistic in comparison to the corresponding NCEP solution. Finally, its reliability is discussed in terms of the implications of the vapor transport features for the El Niño–La Niña transition, vis-à-vis north–south and east–west circulations and their accompanying impact on the atmospheric hydrological cycle.

1. Introduction

One of the important problems in the atmospheric water budget studies is the role of water vapor transport in the atmospheric circulation whose convergence or divergence, in part, shapes spatial distributions of heating through the latent heat release. Because the spatial distribution of the heating is the main force driving the atmospheric circulation, in particular over the Tropics, improved knowledge of water vapor transport is important for a better understanding of our climate system. However, to date, our knowledge is not at a satisfactory

Corresponding author address: Prof. Byung-Ju Sohn, School of Earth and Environmental Sciences, Seoul National University, NS80, Seoul, 151-747 South Korea.
E-mail: sohn@snu.ac.kr

stage to allow us to measure the extent to which the mean or extreme climates are contributed by water vapor transport anomalies or vice versa, in particular, in association with large-scale widespread droughts and floods. The foremost example of such climate extremes is El Niño–Southern Oscillation (ENSO), with interannual variations of rainfall (P), as well as evaporation (E) throughout the Tropics. In this paper, based on the vertically integrated water balance, we diagnose water vapor transports from the satellite-derived ($E - P$) field by applying the method used in Chen et al. (1988) for water vapor transport, and Sohn and Smith (1992, 1993) for heat transport calculation.

Our understanding of the role of water vapor transport in the global hydrological cycle is incomplete, due in large part to the lack of observations of atmospheric hydrological data, in particular, over the oceans where conventional observations are sparse. Although conventional measurements are very helpful in diagnosing regional water vapor transport features and the associated water budget (e.g., McBride et al. 1989), persistent uncertainty exists in measuring water vapor transport for a particular climate event occurring globally on an interannual basis. Long-term statistics of the global water vapor transport were documented based on conventional measurements of dynamic and hydrological variables (Rosen et al. 1979; Peixoto and Oort 1983), but only in a climatological sense with very coarse spatial resolution. Thus, a quantitative measurement of the water vapor transport features associated with warm SST during El Niño may not be achievable, although water vapor convergence into the warm SST area can be expected, as noted in studies explaining the relationships between SST and convection (e.g., Webster 1981; Lindzen and Nigam 1987). Likewise, it is questionable when radiosonde observations are used for assessing water vapor transports from the cold oceans into the surroundings during La Niña. Thus, motivation to improve the quality of water vapor transports over the oceans using spatially and temporally homogeneous satellite measurements is clear.

On the other hand, many atmospheric moisture transport studies have been conducted with the global analyses from assimilation of observed moisture data, by vertically integrating the layer mean moisture flux (e.g., Trenberth and Guillemot 1995; Mo and Higgins 1996; Trenberth and Guillemot 1998; Cohen et al. 2000; Roads et al. 2002). Although the results obtained describe the known climate features reasonably well, this method carries the assumption that the moist physics employed in the model is realistic and accurate. Chen and Pfaendtner (1993) combined satellite-derived precipitation with water vapor flux divergence from model analysis, and then deduced evaporation as a residual. Despite a general resemblance in shape with known evaporation climatologies, discrepancies are substantial—see their Figs. 1 and 2—indicating that the model approach needs improvement to reduce the uncertainties in the global hydrological cycle. These results are consistent with a recent study of Nanjundiah (2000) that showed substantial differences in the water budget induced by two different moisture transport schemes in the National Center for Atmospheric Research (NCAR) Community Climate Model version 2 (CCM2), and with water budget studies over the river basins (Roads et al. 1994; Gutowski et al. 1997; Roads et al. 2002), showing that atmospheric transports from reanalysis data are unable to resolve the water balance inferred from streamflow data over the river basins in the United States.

The above-mentioned deficiencies motivate the use of indirect calculation methods in which the horizontal divergence of water vapor is inferred by satellite-derived water budget data. Apart from conventional measurements and the model reanalysis approach, the steady maturation of passive microwave measurements from space, such as the Special Sensor Microwave Imager (SSM/I) onboard the Defense Meteorological Satellite Program (DMSP) satellite and the Tropical Rainfall Measurement Mission (TRMM) Microwave Imager (TMI) offers an opportunity of studying the atmospheric water budget, including water vapor transport. This is because satellites can now measure various water budget variables like water vapor and precipitation, in addition to the global coverage of near-surface wind, surface-level humidity, and sea surface temperature, which are necessary for the calculation of latent heat flux, with consistent quality and high temporal sampling frequency. Some of these are not generally obtainable from conventional ship measurements. Therefore, it is possible to carry out a purely satellite-based water budget over the global oceans, which in essence captures most of the important water budget components, including water vapor transport. However, the accuracy of spaceborne water budget data may still be questionable in understanding the water budget quantitatively; for example, discrepancies in microwave-based rain estimates are substantial (see Smith et al. 1998; Kummerow et al. 2000). Possible uncertainties influenced by uncertain values of P and E will be addressed in the sensitivity test of section 5.

In this paper, we develop a method of diagnosing the water vapor transport over the global oceans using the above-mentioned satellite-derived water budget parameters, without requiring three-dimensional information on the wind and moisture. The method developed will then be applied to the diagnosis of the long-term features of large-scale water vapor transport [in this study, 7-yr (1988–94) January–February–March (JFM) mean climatology]. Then, the 7-yr mean climatology obtained will serve as a reference transport field for examining the transport features formed in extreme climate events over the Tropics, that is, El Niño and La Niña. In doing so, we examine back-to-back JFM periods of 1998 and 1999 representing the 1997/98 El Niño and the 1999/2000 La Niña.

Section 2 of this paper describes the transport-solving

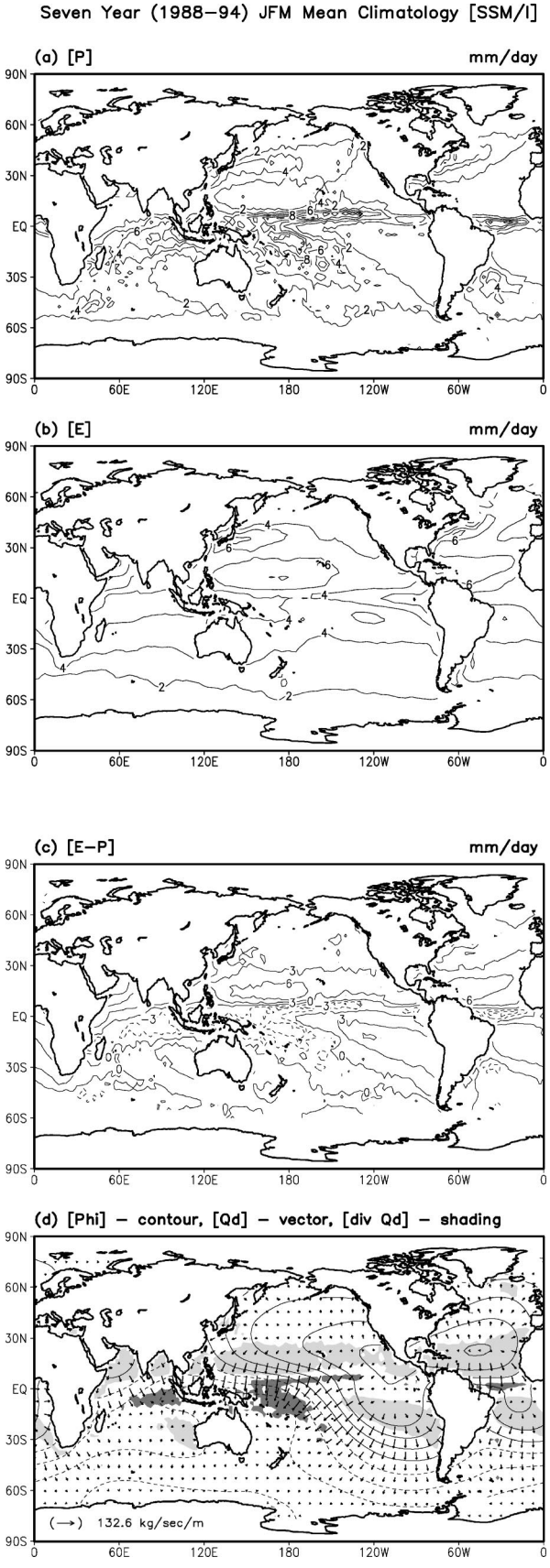

methodology while section 3 describes the datasets used in the study. Section 4 presents the results of the study consisting of the 7-yr JFM mean climatology of water vapor transport, deduced from the SSM/I-derived precipitation and evaporation, along with results from National Centers for Environmental Prediction (NCEP) reanalysis. Sensitivity of water vapor transport to the chosen $[E - P]$ field is discussed in section 5, and transport fields for the ENSO event and a discussion, including the relationships between transports and concurrent SST anomalies, are presented in section 6. Conclusions follow.

2. Methodology

For a given atmospheric column, the water balance achieved can be expressed by the following equation:

$$\frac{\partial(W + W_c)}{\partial t} + \text{div}(\mathbf{Q} + \mathbf{Q}_c) = E - P, \qquad (1)$$

where $W + W_c$ and $\mathbf{Q} + \mathbf{Q}_c$ are the column-integrated total water content and horizontal water flux vector, respectively, and given by

$$W + W_c = \int_0^{P_0} (q + q_l)\,\frac{dp}{g} \qquad (2)$$

$$\mathbf{Q} + \mathbf{Q}_c = \int_0^{P_0} (q + q_l)\mathbf{V}\,\frac{dp}{g}, \qquad (3)$$

where q is the specific humidity, q_l is the liquid-water mixing ratio, and $\mathbf{V}$ is the horizontal wind vector. In Eq. (1), E and P denote evaporation and precipitation, respectively, and the subscript "c" denotes the liquid and ice condensation phases of water vapor.

Often, condensation terms are small, and under those conditions the horizontal divergence of cloud condensates can be neglected. Thus, Eq. (1) is simplified over a specified time period (specified by angle brackets),

$$\left\langle \frac{\partial(W + W_c)}{\partial t} \right\rangle + \langle \text{div}\mathbf{Q} \rangle = \langle E - P \rangle. \qquad (4)$$

When Eq. (4) is integrated over a specific domain of interest, we obtain the time- and space-averaged water balance equation, that is,

←

FIG. 1. SSM/I-derived 7-yr (1988–94) JFM mean (a) precipitation $[P]$, (b) evaporation $[E]$, (c) evaporation minus precipitation $[E - P]$, and (d) divergent water vapor transport $[\mathbf{Q}_D]$ (arrow) embedded with water vapor transport potential function $[\Phi]$ (solid line) and water vapor flux divergence $[\text{div}\mathbf{Q}_D]$ (shaded area). The contour intervals of $[P]$, $[E]$, $[E - P]$, and $[\Phi]$ are 2 mm day^{-1}, 2 mm day^{-1}, 3 mm day^{-1}, and 5.0×10^7 kg s^{-1}, respectively. In (d), heavily shaded and lightly shaded areas represent water vapor flux convergence and divergence greater than 3.5 mm day^{-1}, respectively.

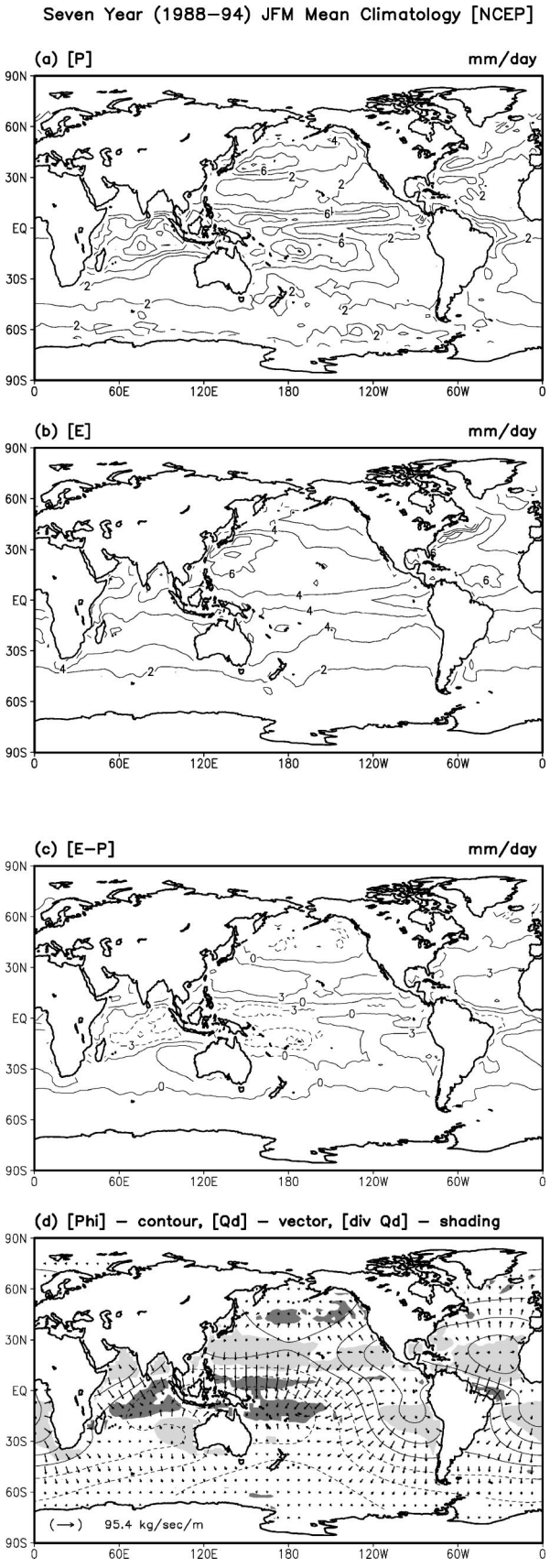

$$\left[\frac{\partial(W + W_c)}{\partial t}\right] + [\mathrm{div}\mathbf{Q}] = [E - P], \tag{5}$$

where brackets denote the spatial averaging operator over a given area A,

$$[X] = \frac{1}{A}\int \langle X\rangle \, dA. \tag{6}$$

Traditionally, large-scale water vapor transport [**Q**] has been derived directly from atmospheric circulation statistics in which transport processes are separated into mean and eddy motions (Peixoto and Oort 1992). Thus, detailed and accurate calculations of three-dimensional mean and eddy transport terms over the globe are required. Notably, the lack of systematically spaced conventional measurements of meteorological variables over oceans has hindered the understanding of features and consequences related to water vapor transport in the hydrological cycle. This motivates the use of indirect calculation methods in which the horizontal divergence of water vapor is balanced by the evaporation minus the precipitation, $[E - P]$, assuming that the rates of change of precipitable water and condensates are small over a sufficiently long period, that is,

$$[\mathrm{div}\mathbf{Q}] = [E - P]. \tag{7}$$

In this study, by introducing the water vapor transport potential function (Φ) and separating the water vapor transport into rotational ($\mathbf{Q}_R$) and divergent ($\mathbf{Q}_D$) components, as in Rosen et al. (1979), Chen (1985), and Sohn and Smith (1992), water vapor transport is solved for, that is,

$$\mathrm{div}\mathbf{Q} = [E - P] = -\nabla^2\Phi \tag{8}$$

$$[\mathbf{Q}_D] = -\nabla\Phi. \tag{9}$$

Equations (8) and (9) are solved on a complete global domain using the spectral method. Because the large-scale atmospheric circulation is nondivergent in essence and, thus, large-scale water vapor transports are largely described by the nondivergent component of water vapor transport, approaches using Eqs. (8) and (9) are more suitable for examining the hydrological cycle directly linking source to sink regions. For example, water vapor transports associated with local Hadley and Walker circulations and their interannual variations can be well conceived by the transport patterns obtained from this approach.

←

FIG. 2. Same as in Fig. 1, but derived from NCEP reanalysis. The contour intervals of $[P]$, $[E]$, $[E - P]$, and $[\Phi]$ are 2 mm day^{-1}, 2 mm day^{-1}, 3 mm day^{-1}, and 3.0×10^7 kg s^{-1}, respectively. In (d), heavily shaded and lightly shaded areas represent water vapor flux convergence and divergence greater than 2.5 mm day^{-1}, respectively.

3. Description of datasets

To solve Eqs. (8) and (9) for the potential function and associated divergent transport vector, the global distribution of evaporation minus precipitation [$E - P$] is required. We use various satellite and reanalysis data, depending upon the objectives.

First, examining mean transport climatology, 7-yr (1988–94) JFM precipitation data are extracted from SSM/I measurements (Wentz and Spencer 1998; see the Web site online at http://www.ssmi.com for a detailed description of the dataset). Evaporation data are from Chou's (1993) product based upon an algorithm that solves the stability-dependent transfer coefficients for the bulk aerodynamic formula iteratively with latent, sensible, and momentum fluxes. Because SSM/I data were mainly used for the evaporation retrieval, we refer to Chou's product as the SSM/I evaporation. Also employed are precipitation and evaporation data obtained from NCEP reanalysis for the comparison of satellite-derived 7-yr mean transport with that derived from reanalysis data.

Second, examining how the water vapor transports obtained are sensitive to chosen precipitation and evaporation datasets, two more 7-yr precipitation datasets and three more evaporation datasets are included, in addition to the SSM/I and NCEP P and E data. They are the 7-yr (1988–94) mean precipitation climatologies from the Global Precipitation Climatology Project (GPCP; see Hufmann et al. 1997) data, and from the European Centre for Medium-Range Weather Forecasts (ECMWF) analysis products; evaporation climatologies are from the Hamburg Ocean–Atmosphere Parameters and Fluxes from Satellite Data (HOAPS; Schulz et al. 1997), an ocean flux dataset (da Silva et al. 1994) based on the Comprehensive Ocean–Atmosphere Data Set (COADS). Thus, for the sensitivity study in section 5, five sets of evaporation data are combined with four different precipitation climatologies, forming, in total, 20 sets of evaporation minus precipitation [$E - P$] fields from which 20 different water vapor transport fields are derived.

Third, for examining the interannual variation of vapor transport occurred during the JFM 1998 El Niño and the JFM 1999 La Niña, we combine SSM/I evaporation with rainfall data obtained from the TRMM Web site (available online at http://trmm.gsfc.nasa.gov). The TRMM products employed were produced by a combination of the various available data sources, that is, a monthly average unclipped TMI estimate, monthly average SSM/I estimate, pentad geostationary infrared (IR) estimate, and the monthly accumulated Climate Assessment and Monitoring System (CAMS) or Global Precipitation Climatology Center (GPCC) rain gauge analysis. The merged data (referred to as the 3B-43 dataset) are then binned into a $1° \times 1°$ grid in the 40°N–40°S domain. In order to cover the whole oceans, SSM/I-derived precipitation data are used 40° poleward in both hemispheres where infrared–microwave merged data are not available.

4. Properties of 7-yr water vapor transport solution

In this section, we examine the 7-yr (1988–94) JFM mean atmospheric hydrological parameters derived from the SSM/I measurements, which will then serve as a reference JFM climate. Because SSM/I-estimated $E - P$ data are available only over the ocean, either specified boundary conditions for the transport potential function (Φ) across the continental boundary or the value of the global $E - P$ field is necessary for solving Eq. (8). Instead of specifying arbitrary values for potential functions along the continental boundaries, we use NCEP $E - P$ data over the land to yield a complete global $E - P$ field, so as to avoid boundary value problems in the spherical harmonics approach.

The satellite-derived 7-yr JFM means of P, E, $E - P$, and $\mathbf{Q}_D$ with Φ and div($\mathbf{Q}_D$) are presented in Figs. 1a–1d, respectively. Prominent features found in the precipitation map (Fig. 1a) include local maxima over the intertropical convergence zone (ITCZ) north of the equator from the western Pacific Maritime Continent to the eastern Pacific, over the equatorial Atlantic, over the South Pacific convergence zone (SPCZ) stretching from New Guinea southeastward to about 40°S, 120°W, and over the zone extending from Madagascar to west Sumatra. Also noted are the heavy precipitation areas along the Northern Hemispheric storm tracks in the midlatitudes of the North Pacific and Atlantic Oceans, the South American convergence zone (SACZ) off southern Brazil. On the other hand, minimum precipitation areas are located over the subtropical North Pacific, and over cold oceans off the west coasts of the Southern Hemispheric continents, that is, South Africa, Australia, and South America.

Seven-year JFM mean evaporation is given in Fig. 1b. Maximum evaporation rates larger than 6 mm day^{-1} are found over the North Pacific off East Asia and over the North Atlantic off North America, because of the frequent dry and cold-air advection from the continents eastward onto the warm oceans during the JFM period. Evaporation rates larger than 6 mm day^{-1} are also found in the subtropical trade wind zones over the North Pacific and Atlantic Oceans. It is of interest to note that minimum evaporation areas over the Tropics are generally found to be located with precipitation maximum areas. Zonally extended patterns are noticeable in the Southern Hemispheric oceans.

The difference between evaporation and precipitation ($E - P$) is given in Fig. 1c. The water vapor source ($E - P > 0$) regions are situated in the subtropics of the North Pacific and the North Atlantic, and three cold oceanic areas in the Southern Hemisphere, while sinks ($E - P < 0$) are located in the equatorial convective zones. General patterns are similar to those noted in

precipitation, and the similarity is largely due to the fact that precipitation behaves in a highly localized fashion while evaporation shows large-scale behavior, implying that the spatial patterns of vapor flux convergence (or divergence) are mainly controlled by the spatial distributions of precipitation. The global mean of $E - P$ must be zero for Eq. (8) to be solvable because the area integral of div$\mathbf{Q}$ of Eq. (8) vanishes at the pole. In order to satisfy the balance requirement as given in Eq. (8), the global mean bias of 15.5 W m^{-2} (corresponding to 0.54 mm day^{-1}) is subtracted from the $E - P$ field to yield a zero global mean, while preserving the spatial gradient of $[E - P]$.

The resultant divergent component of water vapor transport ($\mathbf{Q}_D$) is illustrated in Fig. 1d, along with the potential function [Φ], and divergence [div$\mathbf{Q}_D$]. Because the spatial gradient of the potential function gives rise to a water vapor flux whose divergence must be equal to $[E - P]$ to satisfy a steady-state condition, the overall pattern of the potential function is analogous to the $[E - P]$ field, but has a much smoother shape because of the Laplacian operator. As in Eq. (9), the cross gradient of [Φ] yields the divergent component of transport whose convergence (dark shadings) and divergence (light shadings) represent moisture sink and source, respectively.

In the Pacific, the ridges of the potential function extend from the eastern Pacific to the East China Sea, and to the southeast Pacific, in contrast to the trough from Madagascar to the east of New Guinea. Such distributions of ridge and trough establish a great southward transport band extending from the equatorial Indian Ocean to the southeast Pacific through the Maritime Continent and the central Pacific. In the Atlantic, a high-potential area centered over the east of the West Indies and a local high in the south mid-Atlantic form a relatively strong vector transport across the equator.

Overall, southward moisture transport from the subtropical northwestern Pacific to the western Pacific warm pool region appears to be the main mechanism resulting in the maximum vapor flux convergence and, thus, precipitation over the western Pacific. In addition, the moisture convergence is also attributed to the westward transport from the tropical eastern Pacific west of 120°W, in response to the Walker circulation. Thus, the distributions of water vapor transport and their associated moisture convergence or divergence are in good agreement with what can be expected from the climatologically known Hadley and Walker circulations over the Tropics. Overall, the Northern Hemispheric subtropical oceans and the eastern Pacific serve as moisture source regions, while evaporated moisture is mainly carried into deep moisture sink convective regions, such as ITCZ and SPCZ, by the lower-tropospheric branches of the Hadley and Walker circulations.

Corresponding P, E, $E - P$, and $\mathbf{Q}_D$ values from NCEP reanalysis are given in Fig. 2, for the comparison with satellite estimates. Large-scale features are in general agreement with those from SSM/I estimates, although differences are significant over some areas. Along the ITCZ, precipitation magnitudes are smaller and heavy rain areas (>6 mm day^{-1}) are broader. The precipitation zone associated with the SPCZ is also broader and extends far to the east, so the amount of rainfall over the cold oceans of the southeast Pacific is substantially larger than what is suggested from satellite observations. Measurable differences in evaporation are found over the subtropical North Pacific and the southeastern Pacific off the Peruvian coast.

The resultant $E - P$ field and moisture flux divergence show similar patterns to those from SSM/I, for example, features of dominant cross-equatorial transport in the western half of the Pacific Ocean and the Indian Ocean, and westward moisture transport from the eastern Pacific to the Maritime Continent. However, the transport magnitudes are significantly different, considering that the NCEP maximum transport of 95 kg s^{-1} m^{-1} is much smaller than the 132 kg s^{-1} m^{-1} from SSM/I. A notable difference is also found in the location of the SPCZ. The annual mean position of the SPCZ axis stretches from New Guinea east-southeastward to about 30°S, 120°W, and further stretches southeastward with the highest intensity in the southern summer [see Vincent (1994) for a review of the SPCZ]. In contrast to the well-established SPCZ axis in SSM/I $E - P$ and the moisture transport field, NCEP results show a much more zonally elongated SPCZ pattern. In addition to this regional difference, it can be conjectured that differences become significant if major circulation changes occur in the Tropics, particularly in association with ENSO events. These interannual variations of water vapor transport occurring during El Niño and La Niña periods are given in section 6.

5. Sensitivity of transport solutions to different $E - P$ datasets

As suggested in the global mean $E - P$ bias, uncertainties in satellite estimates of $[E - P]$ lead to erroneous water vapor transports. To determine how the results are affected by uncertainties in input parameters, we examine the sensitivity of vector transport to the chosen climatologies by combining four sets of precipitation and five sets of evaporation data, as described in section 3. Zonal averages of meridional components over the global oceans and 10°N–10°S band averages of zonal components are obtained from a total of 20 water vapor transport fields (see Figs. 3a and 3b). In this calculation, mean biases given in Table 1 are removed from respective $[E - P]$ fields, as described in section 4.

We note that precipitation dataset differences have a larger impact on water vapor flux divergence than do different evaporation estimates. Ignoring the transport fields obtained from the HOAPS evaporation data, which appear to be outliers, transport fields are merged

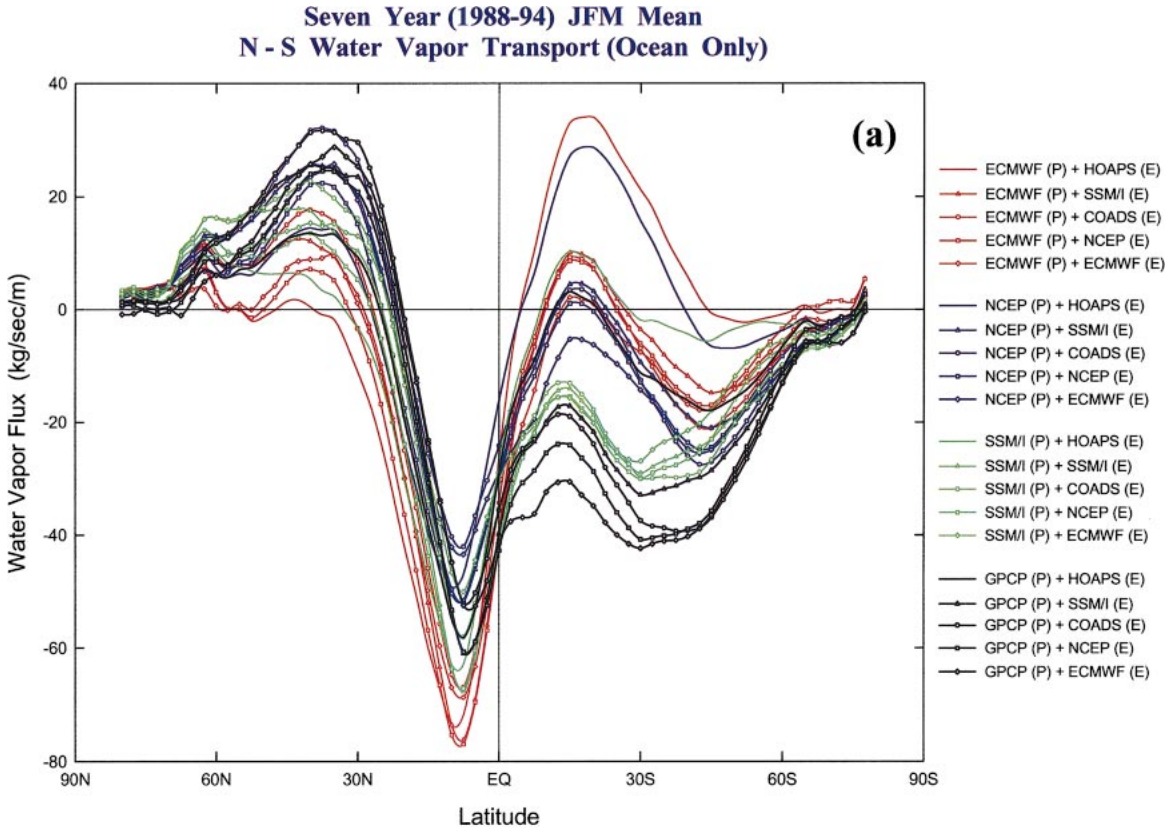
Seven Year (1988-94) JFM Mean
N - S Water Vapor Transport (Ocean Only)
(a)
Water Vapor Flux (kg/sec/m)
Latitude
90N
60N
30N
EQ
30S
60S
90S
40
20
0
-20
-40
-60
-80
ECMWF (P) + HOAPS (E)
ECMWF (P) + SSM/I (E)
ECMWF (P) + COADS (E)
ECMWF (P) + NCEP (E)
ECMWF (P) + ECMWF (E)
NCEP (P) + HOAPS (E)
NCEP (P) + SSM/I (E)
NCEP (P) + COADS (E)
NCEP (P) + NCEP (E)
NCEP (P) + ECMWF (E)
SSM/I (P) + HOAPS (E)
SSM/I (P) + SSM/I (E)
SSM/I (P) + COADS (E)
SSM/I (P) + NCEP (E)
SSM/I (P) + ECMWF (E)
GPCP (P) + HOAPS (E)
GPCP (P) + SSM/I (E)
GPCP (P) + COADS (E)
GPCP (P) + NCEP (E)
GPCP (P) + ECMWF (E)

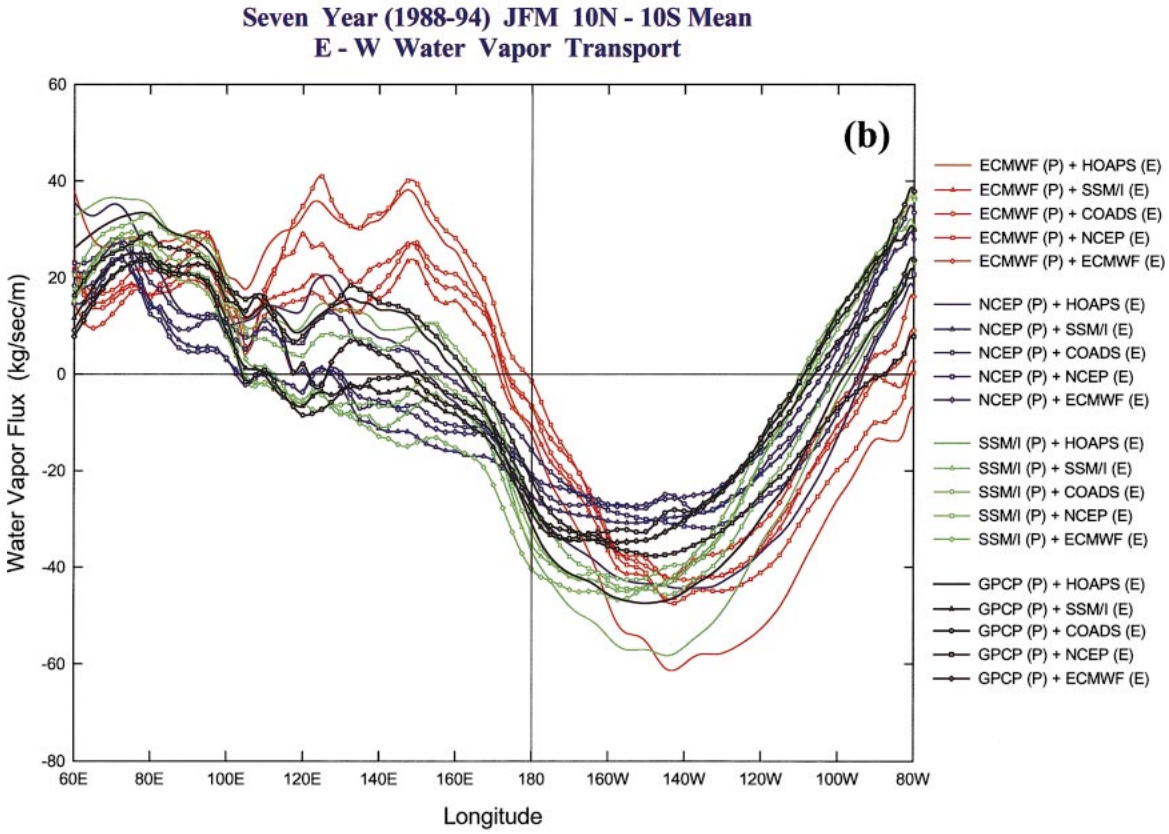
Seven Year (1988-94) JFM 10N - 10S Mean
E - W Water Vapor Transport
(b)
Water Vapor Flux (kg/sec/m)
Longitude
60E
80E
100E
120E
140E
160E
180
160W
140W
120W
100W
80W
60
40
20
0
-20
-40
-60
-80
ECMWF (P) + HOAPS (E)
ECMWF (P) + SSM/I (E)
ECMWF (P) + COADS (E)
ECMWF (P) + NCEP (E)
ECMWF (P) + ECMWF (E)
NCEP (P) + HOAPS (E)
NCEP (P) + SSM/I (E)
NCEP (P) + COADS (E)
NCEP (P) + NCEP (E)
NCEP (P) + ECMWF (E)
SSM/I (P) + HOAPS (E)
SSM/I (P) + SSM/I (E)
SSM/I (P) + COADS (E)
SSM/I (P) + NCEP (E)
SSM/I (P) + ECMWF (E)
GPCP (P) + HOAPS (E)
GPCP (P) + SSM/I (E)
GPCP (P) + COADS (E)
GPCP (P) + NCEP (E)
GPCP (P) + ECMWF (E)

into four groups largely depending on the precipitation climatology employed. This is particularly evident in the Southern Hemisphere where a lesser degree of agreement between transports is noted, in comparison with the Northern Hemisphere. The results from ECMWF precipitation form a bound of the transport packets; that is, the largest equatorward transports occur about 10°N, while the smallest poleward transports are in the Southern Hemisphere. This seems to be due to the fact that the ECMWF model produces too much rain over the tropical warm SST area, in particular over the western Pacific (R. Kelly 2002, personal communication), which dictates more water vapor convergence onto that region and is achieved by larger equatorward transport of water vapor in the Northern Hemisphere. The use of NCEP precipitation tends to generate a transport pattern very similar to ECMWF in the Southern Hemisphere.

In the Southern Hemisphere, the model pair is differentiated from the satellite pair whose poleward transports are much stronger. In fact, near-zero or weak northward transports by the model pair are found near 15°S, whereas 15–30 kg s^{-1} m^{-1} of southward transports are estimated from the satellite pair. Furthermore, the model pair shows a shift of latitude showing the largest southward transport further south. As shown in the NCEP reanalysis results (Fig. 2), the weak southward transports may be attributed to a more prominent northward transport in the Indian Ocean, and dominant westward transport over the central Pacific along 15°S. Based on our assertion that observational biases in satellite-derived [$E - P$] between hemispheres should be small, the striking difference found in the Southern Hemisphere may be due to spatially and temporally limited observations in the Southern Hemispheric oceans employed in the numerical weather prediction model, and, thus, the near-zero and weaker northward transports found in the Southern Hemisphere may be less reliable.

The east–west component of derived water vapor transports, averaged over the equatorial belt from 10°N to 10°S, is given in Fig. 3b. A salient feature in the east–west transport near the equatorial area is westward transports over most of the equatorial Pacific west at about 110°W, indicating that the returning Walker circulation in the lower troposphere carries a substantial amount of water vapor onto the western Pacific. As in the north–south transport, ECMWF also shows extreme results again reflecting too much rain over the warm pool to the central Pacific area and, thus, much water vapor convergence onto that region. Also shown is the outlying pattern caused by the inclusion of HOAPS evaporation data. Excluding ECMWF and HOAPS results, calculated transports are in quite good agreement, although fluctuations are up to 20 kg s^{-1} m^{-1} throughout the equatorial belt.

TABLE 1. The global mean [$E - P$] biases. Units are W m^{-2}.

	Evaporation				
	HOAPS	SSM/I	COADS	NCEP	ECMWF
Precipitation					
ECMWF	−12.14	2.67	4.90	−4.79	−3.91
NCEP	−4.13	10.56	12.87	2.58	3.47
SSM/I	2.49	15.51	18.44	8.75	4.56
GPCP	−4.21	11.62	13.33	3.91	4.79

6. Differences between El Niño and La Niña transports

From the 7-yr mean climatology given in Fig. 1, it was demonstrated that the transport features obtained over the Tropics are consistent with what can be expected from climatologically known thermally driven north–south Hadley and east–west Walker circulations. That is because the moisture sink due to excess precipitation over the western Pacific and the Indian Ocean should be balanced by water vapor convergence associated mainly with low-level branches of those prevalent tropical circulations. So, it is of interest to examine how the major change of climate regime over the Tropics, for example, from the warm to the cold episode, can have an impact on the hydrological cycle, in particular, on moisture transport. With this objective in mind, we examine the interannual variability of the atmospheric water budget, in the framework of El Niño and La Niña, using satellite observations.

Satellite-based precipitation minus evaporation [$E - P$], and the associated moisture transports for JFM 1998 are presented in Fig. 4a,b for El Niño. The precipitation pattern during El Niño (not shown) shows increased rainfall over the central Pacific, and reduced rainfall in the SPCZ and the tropical western Pacific. On the other hand, distributions of evaporation (not shown) exhibit substantially increased moisture influx to the atmosphere over the subtropical oceans, especially in the North Pacific. Taking rainfall together with evaporation, a north–south-aligned [$E - P$] field shows a dominant zonal pattern in which most of the equatorial oceans in the Southern Hemisphere serve as moisture sinks, while the Northern Hemispheric trade wind zones and Southern Hemispheric cold oceans serve as moisture sources. The strong north–south gradients of [$E - P$] between

←

FIG. 3. Seven-year (1988–94) JFM mean (a) meridional component of water vapor flux over the global oceans, and (b) zonal component averaged over the 10°N–10°S latitude band over ocean, obtained from 20 combinations from four sets of precipitation data (SSM/I, GPCP, NCEP, and ECMWF) and five sets of evaporation data (SSM/I, COADS, HOAPS, NCEP, and ECMWF). Symbols for the 20 combinations are given in the right-hand side of the figure.

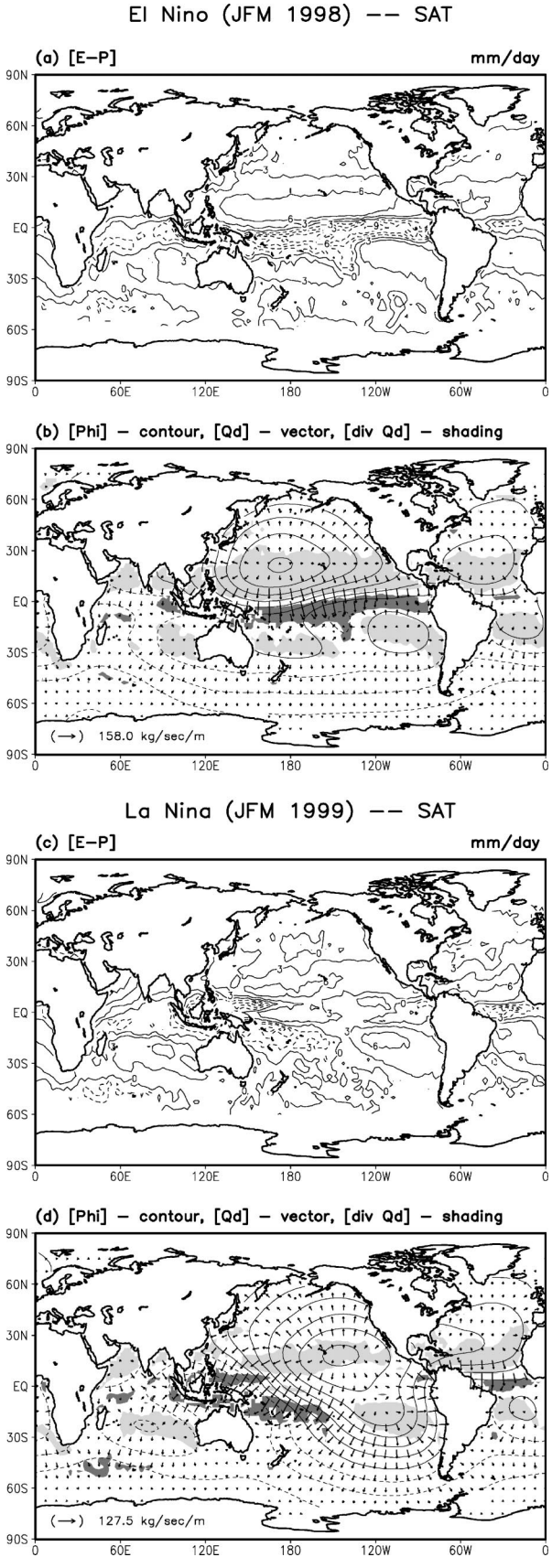

source and sink regions imply that Hadley-type circulation is intensified, connecting more vigorous upward motion in the equatorial region with the strengthened sinking motion over the North Pacific, as shown in Oort and Yienger (1996).

As expected from the $[E - P]$ distribution, the derived transport vector delineates predominant and strong southward transport over most of the tropical North Pacific (cf. with the 7-yr mean climatology given in Fig. 1d). Thus, it appears that the subtropical North Pacific serves as a major moisture source region, while most of the equatorial oceans in the Southern Hemisphere act as a moisture sink region. The foremost differences in the climatology are found in the eastern Pacific where the southward transport connecting the source region to the sink region is well established during the 1998 warm episode. Also noted is that southward water vapor fluxes diverging from the eastern Pacific cold ocean, as shown in Fig. 1, were much weakened, in fact giving rise to a weak northward transport over the eastern equatorial Pacific. A notable feature found in the midlatitudes is strengthened northward transport in the Northern Hemisphere, suggesting that eddy activities transporting water vapor poleward may be increased in the North Pacific during the winter of the warm event.

Distributions of $[E - P]$ and moisture transport for JFM 1999 (La Niña) are given in Figs. 4c,d. In contrast to El Niño (JFM 1998), the north–south-aligned $[E - P]$ distribution is now turned into an east–west coupled pattern in which the moisture sink region located in the tropical western Pacific contrasts with the moisture source region in the east Pacific. The derived water vapor transport during La Niña (Fig. 4d) clearly reveals an east–west coupled pattern, transporting water vapor from the eastern Pacific into the western Pacific warm pool region due to the strengthened Walker circulation. In general, however, transport magnitudes appear to be smaller compared to those found during the El Niño event, suggesting that the hydrological cycle is enhanced during the El Niño event.

Despite strikingly different transport patterns between El Niño and La Niña events, the subtropical oceans in both hemispheres serve as moisture source regions during both events. During El Niño, high-transport potential function areas are located over the subtropics in both hemispheres, but separated by a low potential area over the equatorial region. By contrast, during La Niña, high-potential areas in both subtropical oceans are merged

←

FIG. 4. Satellite-derived (a) evaporation minus precipitation $[E - P]$, and (b) divergent water vapor transport $[\mathbf{Q}_D]$ (arrow) with potential function of water vapor transport $[\Phi]$ (contour) for El Niño (JFM 1998). (c), (d) Same as in (a) and (b), but for La Niña (JFM 1999). The contour intervals of $[E - P]$, and $[\Phi]$ are 3 mm day^{-1}, and 5.0×10^7 kg s^{-1}, respectively. In (b) and (d), heavily and lightly shaded areas represent water vapor flux convergence and divergence greater than 3.5 mm day^{-1}, respectively.

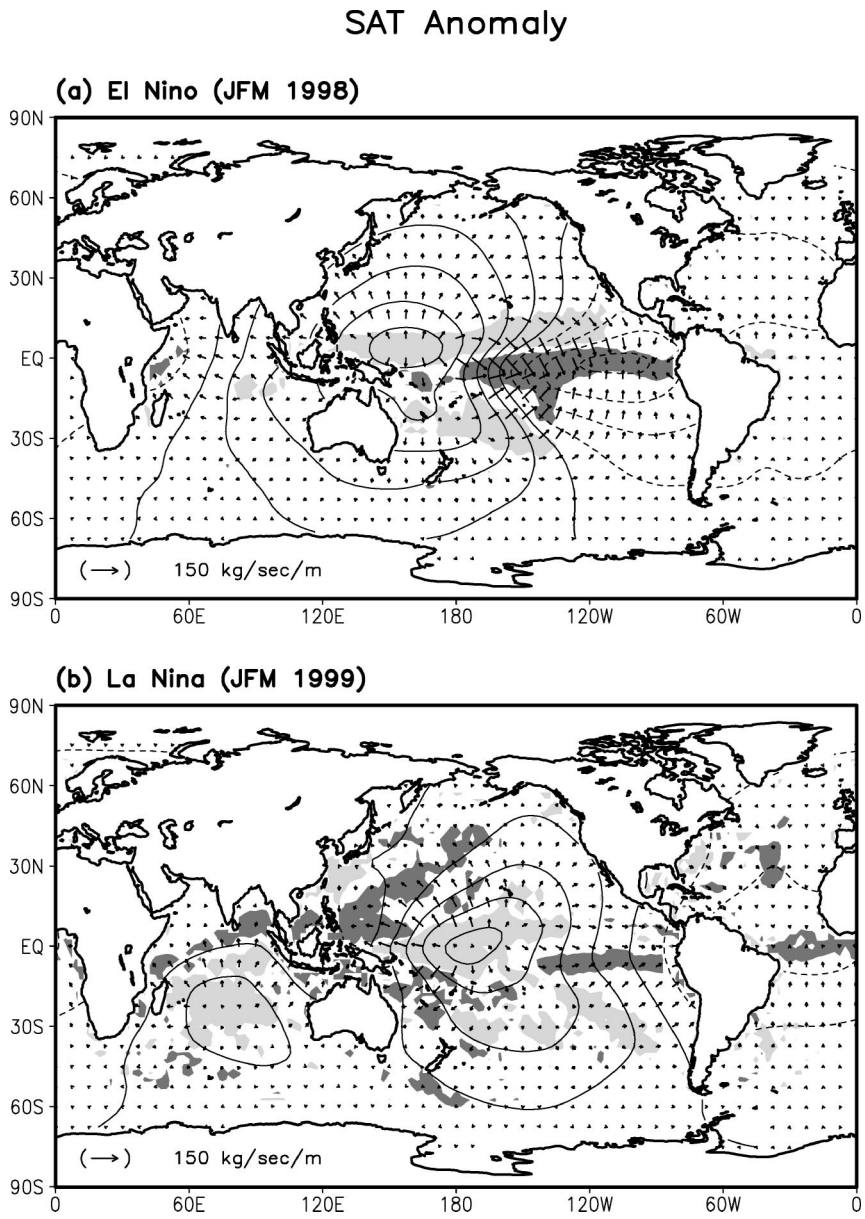

FIG. 5. Anomalies of divergent water vapor transport (arrow) with potential function anomalies (contour) derived from satellite measurements for (a) El Niño (JFM 1998) and (b) La Niña (JFM 1999). The contour intervals of potential function anomalies are 5.0×10^7 kg s^{-1}. Heavily and lightly shaded areas represent water vapor flux convergence and divergence greater than 3.5 mm day^{-1} for (a) El Niño, and greater than 2 mm day^{-1} for (b) La Niña.

and located over the east Pacific, establishing a dipole-like pattern in which the high in the eastern Pacific and the low in the western Pacific are formed.

Figure 5 shows distributions of moisture transport anomaly, together with potential function and transport-induced flux convergence anomalies. Anomalies are obtained by taking the difference from the 7-yr JFM mean given in Fig. 1d. Results indicate that there are distinct differences in water vapor transport anomalies between El Niño and La Niña. During El Niño, transport anomalies whose magnitudes are comparable to those found in the mean field take place in the eastern half of the tropical Pacific, with strong eastward vapor transports from the date line to the equatorial eastern Pacific, and equatorward transport from the subtropics of both hemispheres. The magnitudes of east–west and north–south transport anomalies over the tropical eastern Pacific appear to be comparable to each other. The spatial structure and magnitudes of water vapor transport noted in Fig. 5a reflect circulation variability in the Tropics during

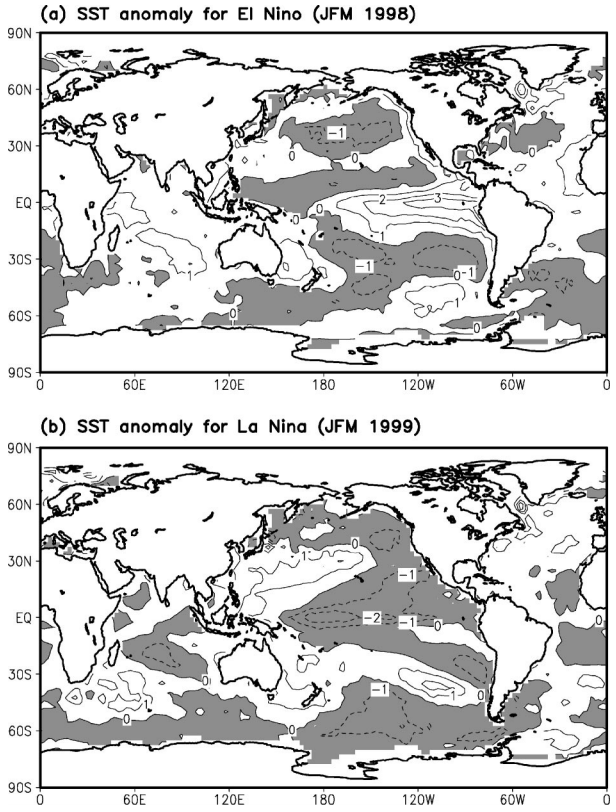

FIG. 6. SST anomalies for (a) El Niño (JFM 1998) and (b) La Niña (JFM 1999). The contour interval is 1°C, and shaded area represent negative SST anomalies.

El Niño, that is, strengthened Hadley and weakened Walker circulation (Philander 1990; Oort and Yienger 1996).

Unlike with the El Niño phase, JFM 1999 shows that the central tropical Pacific serves as an anomalous vapor source region, transporting moisture westward into the western Pacific warm pool region, as well as eastward into the eastern Pacific ITCZ area. Much weakened equatorward transports are noted in the eastern Pacific during La Niña, compared to El Niño in the previous JFM period, reflecting weakened Hadley circulation. Also found is the much weaker eastward transport over the eastern Pacific where strong moisture flux and associated vapor convergence are noted.

There have been attempts to understand atmosphere–ocean interaction processes, in response to the surface heat source associated with SST anomalies. For example, Lindzen and Nigam (1987) argued that the existence of the ITCZ in the western and central Pacific owes to underlying SST gradients because SST gradients impose pressure gradients that, in turn, drive low-level winds and, thus, moisture convergence. They further stated that maximum moisture convergence tends to take place where SST gradients are greatest. In this regard, it is of interest to examine how moisture flux anomalies are correlated to underlying SST anomalies over the eastern Pacific where most dramatic changes in SST and convection take place during the ENSO event. Our expectation is that moisture fluxes shown in Figs. 5a and 5b are closely linked to SST anomalies.

For the examination of possible relationships, SST anomalies for JFM 1998 and JFM 1999 are given in Fig. 6. The SST anomalies for JFM 1998 are similar to typical ENSO SST anomalies, showing positive anomalies with a maximum up to 3°C over the equatorial eastern Pacific and negative anomalies surrounding the positive anomaly area, with a horseshoe shape over the western Pacific and the adjacent subtropics in both hemispheres. It is noted that the maximum flux convergence zone over the equatorial central Pacific is nearly coincident with the ridge of positive SST anomaly (cf. with the darkly shaded area in Fig. 5a with positive SST anomaly area in the eastern Pacific). On the other hand, the highest potential anomaly areas (or water vapor divergence areas) over the Tropics tend to be associated with a negative anomaly area. Despite the comparison being made only over the area showing significant SST changes over the Tropics, the near agreement of the moisture convergence area with the high SST anomaly area strongly suggests that the transport results obtained in this study support the theory proposed by Lindzen and Nigam (1987).

During La Niña, most of the tropical central Pacific to the eastern Pacific shows negative anomalies, with a maximum SST anomaly up to −2°C near the date line. Although the hypothesis proposed by Lindzen and Nigam may not be directly applicable to an area undergoing a cooling process, it is worthy of noting that the maximum negative SST anomaly area is coincident with the highest potential anomaly area.

In comparison to satellite-derived patterns, transport anomalies from NCEP reanalysis show similar large-scale features during El Niño, for example vapor flux convergence onto the equatorial central Pacific to the eastern Pacific, and flux divergence over a surrounding horseshoelike area (see Fig. 7). Unlike with satellite results showing the axis of water vapor convergence along the ridge of positive SST anomaly, the convergence axis appears to be located further south, roughly along the 10°S line of latitude. Also found are strong equatorward transports west of the date line over the equatorial region where near-zero SST anomalies and small satellite-derived transports are observed. Furthermore, the magnitudes of transport anomalies from the NCEP reanalysis are much smaller than suggested by satellite-based $[E - P]$, suggesting a weaker hydrological cycle in NCEP reanalysis.

During La Niña, transport anomalies of NCEP reanalysis exhibit a wavenumber 2 pattern, in which the Indian Ocean and central Pacific serve as anomalous moisture sources, whereas the western Pacific and South America serve as sinks. Strong northward and northwestward transports shown in satellite-based results tend to be very weak and obscured, and a maximum negative

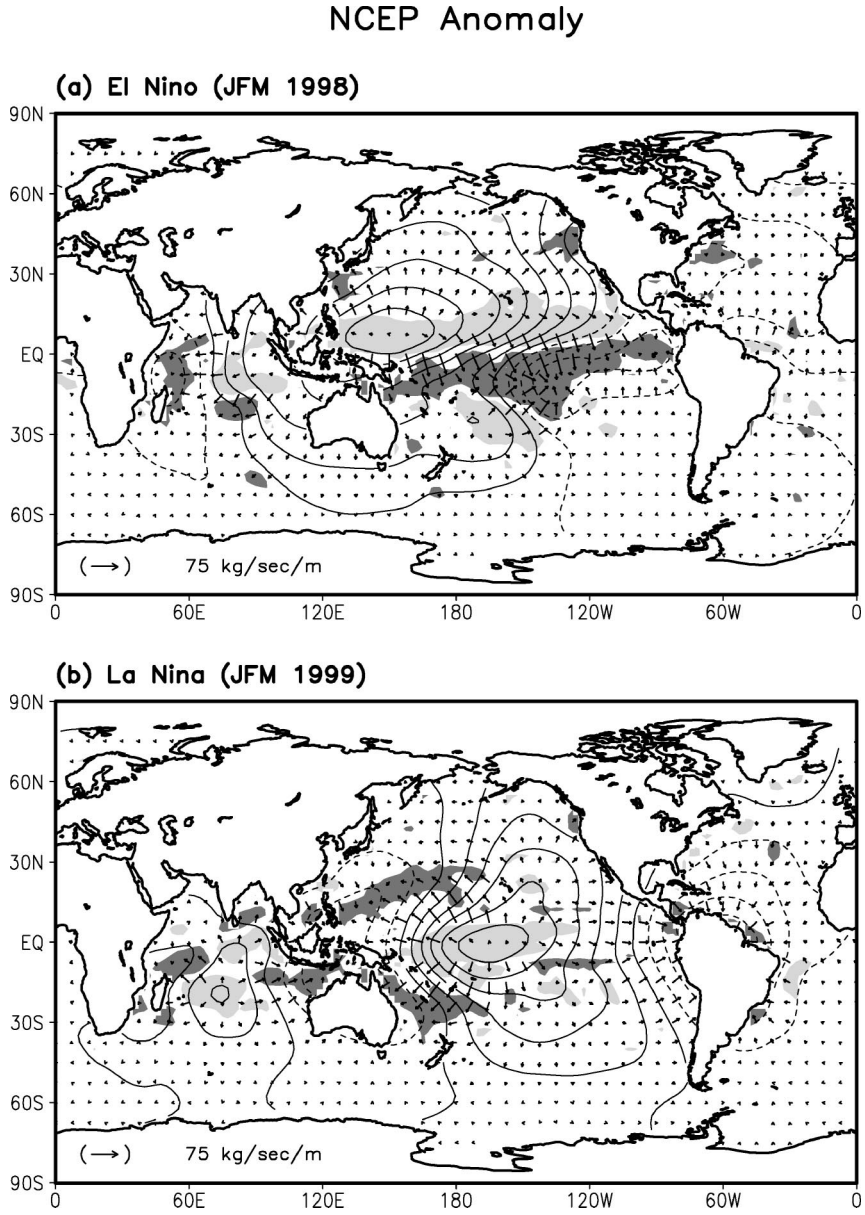

FIG. 7. Same as in Fig. 5, except derived from NCEP reanalysis. The contour intervals of potential function anomalies are 2.0×10^7 kg s^{-1}. Heavily and lightly shaded areas represent water vapor flux convergence and divergence greater than 2 mm day^{-1} for both (a) El Niño and (b) La Niña.

SST anomaly area over the date line is no longer coincident with the highest potential anomaly area. As in El Niño, significant differences are noted in transport magnitudes.

7. Conclusions

In this study, a methodology for determining the atmospheric water vapor transport field directly from satellite-retrieved over-ocean $E - P$ datasets is presented and applied to an analysis of the 1998/99 El Niño–La Niña transition to understand the processes and implications of climatically contrasted vapor transport situations. The methodology is based on the solution to a potential function representation of the $E - P$ difference field, using a spectral solution technique that was described in Sohn and Smith (1992, 1993) for determining required global atmosphere–ocean energy transports. For scales under which the atmospheric water budget equation can be reduced to a balance between $E - P$ and div$\mathbf{Q}$ and in which adequate boundary conditions are available at the ocean–continent interfaces, it is ev-

ident that realistic solutions are obtainable for divergent water vapor processes and transports. The analysis shows how and why the anomaly solutions for the 1998–99 El Niño–La Niña events differ, and how the solutions are consistent with SST anomaly conditions during the two events, evidently more consistent than possible with current global analysis products.

Clearly the main advantage of the methodology is that it can approach the problem of determining an important global water cycle process over regions in which wind measurements are sparse, that is, the World Ocean. Moreover, the methodology addresses one of the strengths of satellite measurements, that is, by nature they provide global coverage, consistent coverage, and continuity in sampling. By the same token, the transport solutions are sensitive to gradients within the $E - P$ fields, which means they are sensitive to uncertainties in the satellite retrievals of precipitation and evaporation. In fact, the sensitivity analysis presented in section 5 illustrated just how sensitive zonally averaged vapor transports are to different combinations of P and E datasets—the main result being that it is the difference properties of the current P datasets, more so than the E datasets, that largely control the difference properties of the final transport solutions. By the same token, we noted that the combined SSM/I–TRMM satellite solutions can be considered reliable, relative to various results that depend on model datasets, which have uncertainties in model parameterized physics.

The main difference in water vapor transports between the 1998 and 1999 JFM El Niño and La Niña periods, is the former's largely meridionally aligned circulation and the latter's largely zonally aligned circulation, the contrast resulting from the well-established eastward shift of convection from the west to central Pacific during an active ENSO related to concomitant ocean dynamics and relaxation of the easterly trades. However, there are numerous detailed properties in the two vapor transport solutions that are not immediately recognizable without an understanding of their direct relationship to precipitation and evaporation conditions, which are generally thought of as more of a response to details in the vapor transports than they are a determinant of them. However, because vertically integrated $\mathbf{Q} + \mathbf{Q}_c$ fluxes on a seasonal scale are essentially out of reach, using conventional observations, it is actually more straightforward to solve for the dynamical flux term $\mathbf{Q}_D$ from the hydrological term $E - P$, than vice versa, when considering the problem from a remote sensing perspective. Ideally, of course, a time will come when lidar-retrieved winds from satellites will become a reality and then, with both sides of the balance equation being observable independently, the process of reconciling residual imbalances related to standing uncertainties in the P, E, $\mathbf{V}(p)$, and $q(p) + q_c(p)$ retrievals may commence.

In the meantime, it is important to understand the myriad processes within the global hydrological cycle, particularly seasonal water vapor transports, whose year-to-year variations have such far-reaching consequences on climate dynamics—particularly atmospheric stability, cloudiness, precipitation, and the radiation budget. It is also important to use any available and credible observational means to study the reliability of hydrological processes within general circulation models and to seek invalidation of their underlying formulations until such time as GCMs reproduce detailed processes in water vapor transports with uncertainties no worse than observations. It is fair to say that this situation has yet to occur and, thus, combining satellite-retrieved precipitation and evaporation datasets can help understand both strengths and weaknesses of current-generation GCMs insofar as they circulate water vapor through the atmosphere. Both perspectives motivated this investigation and the interpretation of its results.

Acknowledgments. This research has been supported by the International Cooperation Research Program funded by Ministry of Science and Technology of Korea, and by the BK21 Project of the Korean Government. Part of this research was performed while the first author was resident at NASA MSFC and NASA GSFC as a visiting scientist. F. R. Robertson acknowledges support under the NASA Code YS Global Water and Energy Cycle Program.

REFERENCES

Chen, T.-C., 1985: Global water vapor flux and maintenance during FGGE. *Mon. Wea. Rev.*, **113,** 1801–1919.

——, and J. Pfaendtner, 1993: On the atmospheric branch of the hydrological cycle. *J. Climate,* **6,** 161–167.

——, M.-C. Yen, and M. Murakami, 1988: The water vapor transport associated with the 30–50 day oscillation over the Asian monsoon region during 1979 summer. *Mon. Wea. Rev.*, **116,** 1983–2002.

Chou, S.-H., 1993: A comparison of airborne eddy correlation and bulk aerodynamic methods for ocean-air turbulent fluxes during cold-air outbreaks. *Bound.-Layer Meteor.,* **64,** 75–100.

Cohen, J. L., D. A. Salstein, and R. D. Rosen, 2000: Interannual variability in the meridional transport of water vapor. *J. Hyrometeor.,* **1,** 547–553.

da Silva, A. M., C. C. Young, and S. Levitus, 1994: *Algorithms and Procedures,* Vol. 1. *Atlas of Surface Marine Data 1994, NOAA Atlas NESDIS 6,* U.S. Department of Commerce, 83 pp.

Gutowski, W. J., Jr., Y. Chen, and Z. Ötles, 1997: Atmospheric water vapor transport in NCEP–NCAR reanalyses: Comparison with river discharge in the Central United States. *Bull. Amer. Meteor. Soc.,* **78,** 1957–1969.

Huffman, G. J., and Coauthors, 1997: The global precipitation climatology project (GPCP) combined precipitation dataset. *Bull. Amer. Meteor. Soc.,* **78,** 5–20.

Kummerow, C., and Coauthors, 2000: The status of the Tropical Rainfall Measuring Mission (TRMM) after two years in orbit. *J. Appl. Meteor.,* **39,** 1965–1982.

Lindzen, R. S., and S. Nigam, 1987: On the role of surface sea surface temperature gradients in forcing low-level winds and convergence in the Tropics. *J. Atmos. Sci.,* **44,** 2418–2435.

McBride, J. L., B. W. Gunn, G. J. Holland, T. D. Keenan, N. E. Davidson, and W. M. Frank, 1989: Time series of total heating and moistening over the Gulf of Carpentaria radisonde array during AMEX. *Mon. Wea. Rev.,* **117,** 2701–2713.

Mo, K. C., and R. W. Higgins, 1996: Large-scale atmospheric moisture transport as evaluated in the NCEP/NCAR and the NASA/DAO reanalyses. *J. Climate,* **9,** 1531–1545.

Nanjundiah, R. S., 2000: Impact of the moisture transport formulation on the simulated tropical rainfall in a general circulation model. *Climate Dyn.,* **16,** 303–317.

Oort, A. H., and J. J. Yienger, 1996: Observed interannual variability in the Hadley circulation and its connection to ENSO. *J. Climate,* **9,** 2751–2767.

Peixoto, J. P., and A. H. Oort, 1983: The atmospheric branch of the hydrological cycle and climate. *Variation in the Global Water Budget,* A. Street-Perrott et al., Eds., Reidel, 5–65.

——, and ——, 1992: *Physics of Climate.* American Institute of Physics, 520 pp.

Philander, S. G., 1990: *El Niño, La Niña, and the Southern Oscillation.* Academic Press, 289 pp.

Roads, J. O., S.-C. Chen, A. K. Guetter, and K. P. Georgakakos, 1994: Large-scale aspects of the United States hydrological cycle. *Bull. Amer. Meteor. Soc.,* **75,** 1589–1610.

——, M. Kanamitsu, and R. Stewart, 2002: CSE water and energy budgets in the NCEP–DOE Reanalysis II. *J. Hydrometeor.,* **3,** 227–248.

Rosen, R. D., D. A. Salstein, and J. P. Peixoto, 1979: Variability in the annual fields of large-scale atmospheric water vapor transport. *Mon. Wea. Rev.,* **107,** 26–37.

Schulz, J., J. M. Meywerk, S. Ewald, and P. Schluessel, 1997: Evaluation of satellite-derived latent heat fluxes. *J. Climate,* **10,** 2782–2795.

Smith, E. A., and Coauthors, 1998: Results of WetNet PIP-2 Project. *J. Atmos. Sci.,* **55,** 1483–1536.

Sohn, B. J., and E. A. Smith, 1992: Global energy transports and the influence of clouds on transport requirements: A satellite analysis. *J. Climate,* **5,** 717–734.

——, and ——, 1993: Energy transports by ocean and atmosphere based on an entropy extremum principle. Part I: Zonal averaged transports. *J. Climate,* **6,** 886–899.

Trenberth, K. E., and C. J. Guillemot, 1995: Evaluation of the global moisture budget as seen from analyses. *J. Climate,* **8,** 2255–2272.

——, and ——, 1998: Evaluation of the atmospheric moisture and hydrological cycle in the NCEP/NCAR reanalyses. *Climate Dyn.,* **14,** 213–231.

Vincent, D. G., 1994: The South Pacific Convergence Zone (SPCZ): A review. *Mon. Wea. Rev.,* **122,** 1949–1970.

Webster, P. J., 1981: Mechanisms determining the atmospheric response to sea surface temperature anomalies. *J. Atmos. Sci.,* **38,** 554–571.

Wentz, F. J., and R. W. Spencer, 1998: SSM/I rain retrievals within a unified all-weather ocean algorithm. *J. Atmos. Sci.,* **55,** 1613–1627.